



Atmospheric Erosion by Giant Impacts onto Terrestrial Planets: A Scaling Law for any Speed, Angle, Mass, and Density

J. A. Kegerreis¹ , V. R. Eke¹ , D. C. Catling² , R. J. Massey¹ , L. F. A. Teodoro^{3,4} , and K. J. Zahnle⁵

¹Institute for Computational Cosmology, Durham University, Durham DH1 3LE, UK; jacob.kegerreis@durham.ac.uk

²Department of Earth and Space Sciences, University of Washington, Seattle, WA, USA

³BAERI/NASA Ames Research Center, Moffett Field, CA, USA

⁴School of Physics and Astronomy, University of Glasgow, Glasgow G12 8QQ, UK

⁵NASA Ames Research Center, Moffett Field, CA, USA

Received 2020 July 8; revised 2020 August 19; accepted 2020 August 25; published 2020 September 30

Abstract

We present a new scaling law to predict the loss of atmosphere from planetary collisions for any speed, angle, impactor mass, target mass, and body composition, in the regime of giant impacts onto broadly terrestrial planets with relatively thin atmospheres. To this end, we examine the erosion caused by a wide range of impacts, using 3D smoothed particle hydrodynamics simulations with sufficiently high resolution to directly model the fate of low-mass atmospheres around 1% of the target’s mass. Different collision scenarios lead to extremely different behaviors and consequences for the planets. In spite of this complexity, the fraction of lost atmosphere is fitted well by a power law. Scaling is independent of the system mass for a constant impactor mass ratio. Slow atmosphere-hosting impactors can also deliver a significant mass of atmosphere, but always accompanied by larger proportions of their mantle and core. Different Moon-forming impact hypotheses suggest that around 10%–60% of a primordial atmosphere could have been removed directly, depending on the scenario. We find no evident departure from the scaling trends at the extremes of the parameters explored. The scaling law can be incorporated readily into models of planet formation.

Unified Astronomy Thesaurus concepts: [Earth atmosphere \(437\)](#); [Planetary atmospheres \(1244\)](#); [Impact phenomena \(779\)](#); [Hydrodynamical simulations \(767\)](#)

Supporting material: animation, data behind figure, machine-readable tables

1. Introduction

Terrestrial planets are thought to form from tens of roughly Mars-sized embryos that crash into each other after accreting from a protoplanetary disk (Chambers 2001). At the same time, planets grow their atmospheres by accreting gas from their surrounding nebula, degassing impacting volatiles directly into the atmosphere, and by outgassing volatiles from their interior (Massol et al. 2016).

For a young atmosphere to survive it must withstand radiation pressure of its host star, frequent impacts of small and medium impactors, and typically at least one late giant impact that might remove an entire atmosphere in a single blow (Schlichting & Mukhopadhyay 2018).

The rapidly growing population of observed exoplanets reveals a remarkable diversity of atmospheres, even between otherwise similar planets in the same system (Lopez & Fortney 2014; Liu et al. 2015; Ogihara & Hori 2020), and the Earth’s own atmosphere shows a complex history of fractionation and loss (Tucker & Mukhopadhyay 2014; Sakuraba et al. 2019; Zahnle et al. 2019). However, the full extent of the role played by giant impacts is uncertain, in part due to the lack of comprehensive models for the atmospheric erosion caused across the vast parameter space of possible impact scenarios.

A challenge for numerical simulations is the low density of an atmosphere compared with the planet, which requires high resolution (Kegerreis et al. 2019). For this reason, previous studies have made progress by focusing primarily on 1D models or thick atmospheres ($> \sim 5\%$ of the total mass), often also limited to only head-on impacts or too few scenarios to

make broad scaling predictions (Genda & Abe 2005; Inamdar & Schlichting 2015; Hwang et al. 2018; Denman et al. 2020; Lammer et al. 2020).

Kegerreis et al. (2020, hereafter K20) used high-resolution smoothed particle hydrodynamics (SPH) simulations of giant impacts to investigate the detailed dependence of atmospheric loss on the speed and angle of an impact and to examine the different mechanisms by which thin atmospheres could be eroded. They derived a scaling law to predict the loss from any such collision between an impactor and target similar to those of the canonical Moon-forming impact. However, the study was limited to those single target and impactor masses.

We now simulate a wide range of target and impactor masses and compositions in addition to different angles and speeds, in order to develop a scaling law that can apply to any giant impact in the broad regime of terrestrial planets with thin atmospheres. The tested scenarios include masses ranging from roughly three times the Earth’s mass down to a few percent of its mass; differentiated and undifferentiated planets with densities from about half to over double the Earth’s density; angles from head-on to highly grazing; and speeds from 1 to 3 times the mutual escape speed.

2. Methods

The 259 simulations in this study can be summarized as three related suites: (1) A set of impacts with different target and impactor masses, for head-on and grazing, slow and fast collisions. This also includes some scenarios with atmosphere-hosting impactors. (2) A set of changing-angle and changing-speed scenarios for a subset of target and impactor combinations.

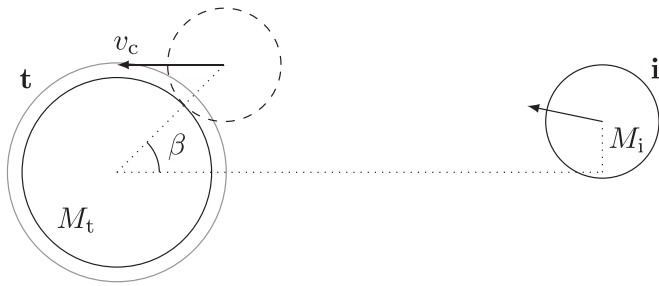


Figure 1. Initial conditions for an impact scenario, with the target (t) on the left and the impactor (i) on the right with masses $M_{t,i}$, shown in the target’s rest frame. The speed and angle at first contact, v_c and β , and the dimensionless impact parameter $b \equiv \sin(\beta)$ are set ignoring the atmosphere and neglecting any tidal distortion before the collision. The initial separation is set such that the time to impact under the same assumptions is 1 hr, using the equations in Appendix A of Kegerreis et al. (2020).

(3) A set of targets and impactors with extreme compositions and densities, including different equations of state. The full details of each suite and the SPH simulations are described in Appendix A. The parameters for each simulation including the resulting atmospheric erosion are also listed in Table 2.

We specify each impact scenario by the masses of the target and impactor, M_t and M_i , in addition to the impact parameter, b , and the speed at first contact, v_c , of the impactor with the target’s surface, as illustrated in Figure 1. The radii, $R_{t,i}$, are defined at the base of any atmosphere. The speed at contact is set in units of the mutual escape speed of the system, $v_{\text{esc}} = \sqrt{2G(M_t + M_i)/(R_t + R_i)}$. For clarity, when used to identify scenarios in the text the M_t and M_i labels do not include any atmosphere.

Our targets and impactors are differentiated into a rocky mantle and an iron core containing 70% and 30% of the mass, respectively, using the Tillotson (1962) granite or, for a subset of 21 simulations, ANEOS forsterite (Stewart et al. 2019) and the Tillotson iron (Melosh 1989) equations of state (EoS). We also use some undifferentiated bodies made of only iron or rock.

All targets and some impactors have an added atmosphere with 1% of their core+mantle mass, using Hubbard & MacFarlane (1980)’s hydrogen–helium EoS. The planetary profiles are generated by integrating inward while maintaining hydrostatic equilibrium,⁶ then the particles are placed to precisely match the resulting density profiles using the stretched equal-area (SEA⁷) method, following the same procedure detailed in K20 Section 2.1.

The simulations are run using the open-source hydrodynamics and gravity code SWIFT⁸ as described in Kegerreis et al. (2019). We use around $10^{7.5}$ SPH particles for each simulation, depending on the masses of the two bodies (see Appendix A). K20 ran convergence tests for the fraction of atmosphere eroded by similar impacts and similar atmosphere mass fractions to those in this study. Simulations using 10^7 particles yielded results that agreed to within $\sim 2\%$ with ones using $10^{7.5}$ and 10^8 particles, with improved convergence for

⁶ The WoMa code for producing spherical and spinning planetary profiles and initial conditions is publicly available with documentation and examples at github.com/srbonilla/WoMa, and the python module `woma` can be installed directly with `pip` (Ruiz-Bonilla et al. 2020).

⁷ The SEAGen code is publicly available at github.com/jkeger/seagen and the python module `seagen` can be installed directly with `pip` (Kegerreis et al. 2019).

⁸ Version 0.8.5. SWIFT is publicly available at www.swiftsim.com.

more-erosive collisions, so our somewhat higher resolution here should be comfortably sufficient.

K20 found that the time required for the amount of eroded material to settle ranges from less than 1 hr after contact for high-speed and/or low-angle impacts up to 5–10 hr for slower, grazing collisions. Depending on the scenario each simulation is run for a conservative 5–14 hr after contact.

3. Results and Discussion

The overall features of these giant impacts vary widely between scenarios, but continue to display the same range of behaviors and erosion mechanisms that was examined in detail by K20. Some of the possible outcomes are illustrated in Figure 2, with the particles that will become gravitationally unbound in the rest frame of the target’s core highlighted in purple. The rows feature: (1) a fast, head-on collision of our smallest impactor onto a small target, resulting in near-total atmospheric loss and significant mantle erosion; (2) a highly grazing impact leaving the target relatively undisturbed while the impactor escapes; (3) a slow, grazing impact of an equal-mass target and impactor, significantly disrupting the planet but not violently enough to actually eject much unbound atmosphere; and (4) a mid-angle collision onto a large target, causing about half of the atmosphere to escape the system along with about half of the impactor.

3.1. Erosion Trends

For a fixed impactor and target, K20 showed that the fraction of lost atmosphere scales as a simple function of the speed and impact parameter. The most important missing pieces are the masses of the target and impactor. We find that the atmospheric erosion depends neatly on the impactor:total mass ratio, as shown in Figure 3 (left panel). Furthermore, the fractional loss has no systematic dependence on the target (or total) mass as long as the impactor mass ratio is the same. These results continue to hold for larger impactors hitting smaller targets and for bodies with different compositions and densities.

The slow, head-on scenarios (blue lines) show significant scatter. This is consistent with the tests in K20 that showed how chaotic this specific type of collision can be, unlike grazing or faster impacts. Even tiny changes in the initial conditions can affect the details of the fall-back and sloshing that occurs after the initial impact and the resulting erosion. This sets a relative uncertainty for these slow, head-on loss estimates of about 20%.

Note that the mass ratio is not varied truly in isolation. Although the other input parameters are kept constant, the speed is set in terms of the escape speed and the angle in terms of the geometry of the system, which depend on the body masses and radii and thus change along with the masses.

We find a similar dependence on the impact angle to that seen by K20, shown in Figure 3 (middle panel) for the second suite of scenarios, including the complex non-monotonic behavior at low angles for slow and smaller impactors. They found that a simple estimate of the fractional volume of the two bodies that interacts can account for any impact angle across the full range of head-on to highly grazing collisions. For the variable bulk densities in this study, we make the minor change to a fractional interacting mass, $f_M(b)$, as detailed in Appendix B, though this modification makes little quantitative

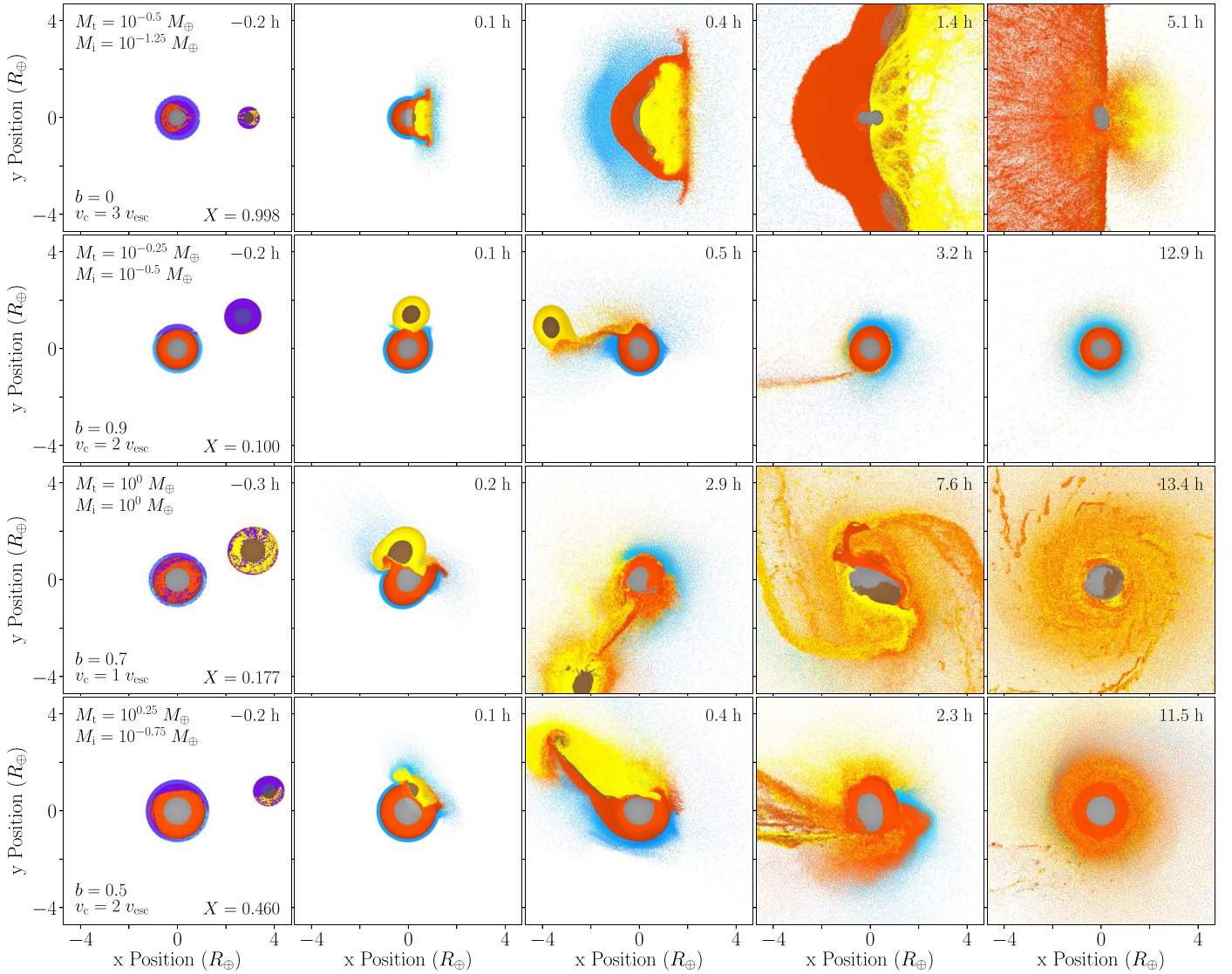


Figure 2. Illustrative snapshot cross-sections from four example impact simulations, using $\sim 10^{7.5}$ SPH particles. The annotations detail the parameters for each scenario (see Section 2 and Figure 1); the lost mass fraction of the atmosphere, X ; and the time. Note that the snapshots are at different times to show the evolution in each case. In the leftmost panels, the particles that will become unbound and escape the system are highlighted in purple on a pre-impact snapshot, though note that less material may be lost away from the impact plane. Gray and orange show the target’s core and mantle material, respectively, and brown and yellow show the same for the impactor. Blue is the target’s atmosphere. The color luminosity varies slightly with the internal energy. An animation is available in the online Journal, showing the early stages of representative slow, fast, head-on, and grazing impacts, with the particles colored by their internal energy.

(An animation of this figure is available.)

difference. These results again appear to be completely independent of the total mass of the system.

The compositions, densities, and internal structures of the planets might also be expected affect the atmosphere loss. With the third suite we test the extreme “terrestrial” cases of undifferentiated pure-iron and pure-rock bodies, keeping either the mass or the radius the same as the standard versions. The overall trends of this suite with the ratio of bulk densities (not including the atmosphere) are shown in Figure 3 (right). The mass ratios and the escape speeds also differ across these scenarios, so it is unsurprising that no perfect scaling appears immediately. Nonetheless, it is promising that some parameterization of the density ratio could align the results across this highly diverse range of bodies and material combinations to a single trend, once the mass and other parameters are accounted for. Figure 3 (left panel) also confirms that these targets and impactors of very different compositions (yellow

lines) still follow the same neat scaling with the mass ratio as the standard cases.

3.2. Scaling Law

We find that the following power law describes the fraction of eroded atmosphere from any impact scenario across this broad regime, as shown in Figure 4:

$$X \approx 0.64 \left[\left(\frac{v_c}{v_{\text{esc}}} \right)^2 \left(\frac{M_i}{M_{\text{tot}}} \right)^{\frac{1}{2}} \left(\frac{\rho_i}{\rho_t} \right)^{\frac{1}{2}} f_M(b) \right]^{0.65}, \quad (1)$$

capped at 1 for total erosion. The prefactor and exponent were found from a least-squares fit to the data points below total loss, with uncertainties of 0.01.

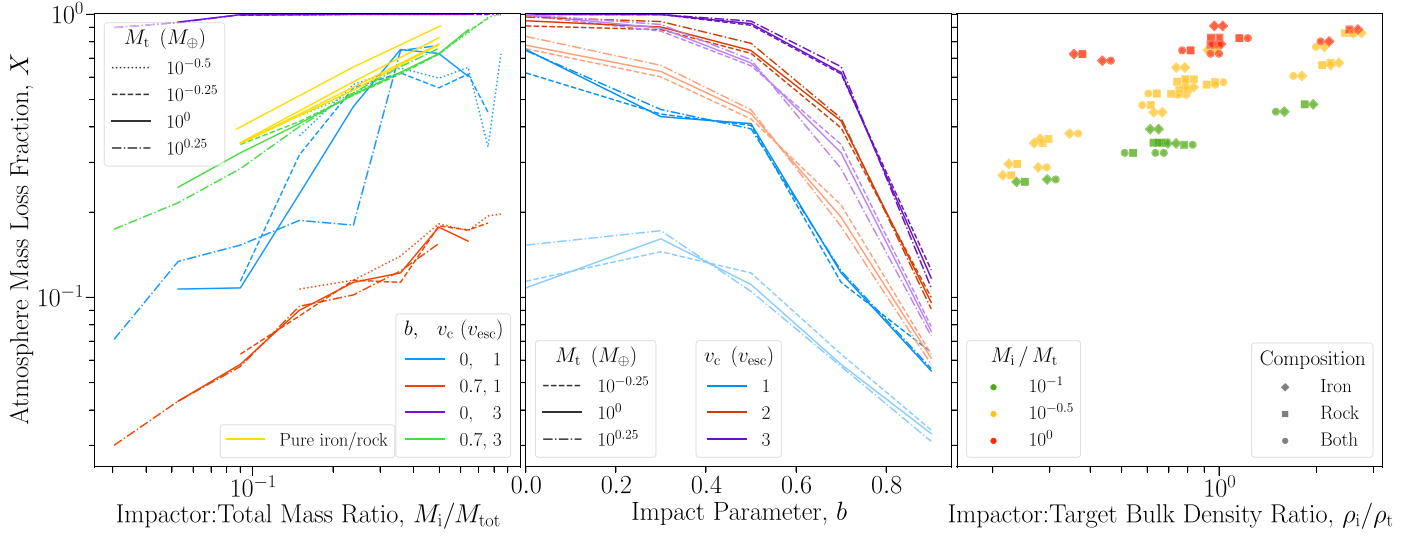


Figure 3. Left panel: lost mass fraction of the atmosphere as a function of the impactor:total mass ratio, plotted separately for each of the four scenarios (colors) and each target mass (line styles) of the first suite, including atmosphere-hosting impactors being treated as targets to give impactor:target mass ratios greater than one. The yellow lines show subsets of the third suite for pure-iron or pure-rock bodies, with $b = 0.7$, $v_c = 3$. Middle panel: lost mass fraction of the atmosphere as a function of the impact parameter, plotted separately for each speed at contact (colors) and each target mass (line styles) of the second suite. The subsets with an impactor:target mass ratio of 10^{-1} are shown by the lighter color (lower magnitude) lines and of $10^{-0.25}$ by the darker lines, respectively. Right panel: lost mass fraction of the atmosphere as a function of the ratio of the impactor and target’s bulk densities, for each base impactor:target mass ratio (colors) of the third suite (see Appendix A). The left and right markers in each pair show the composition of the target and impactor, respectively, as detailed in the legend.

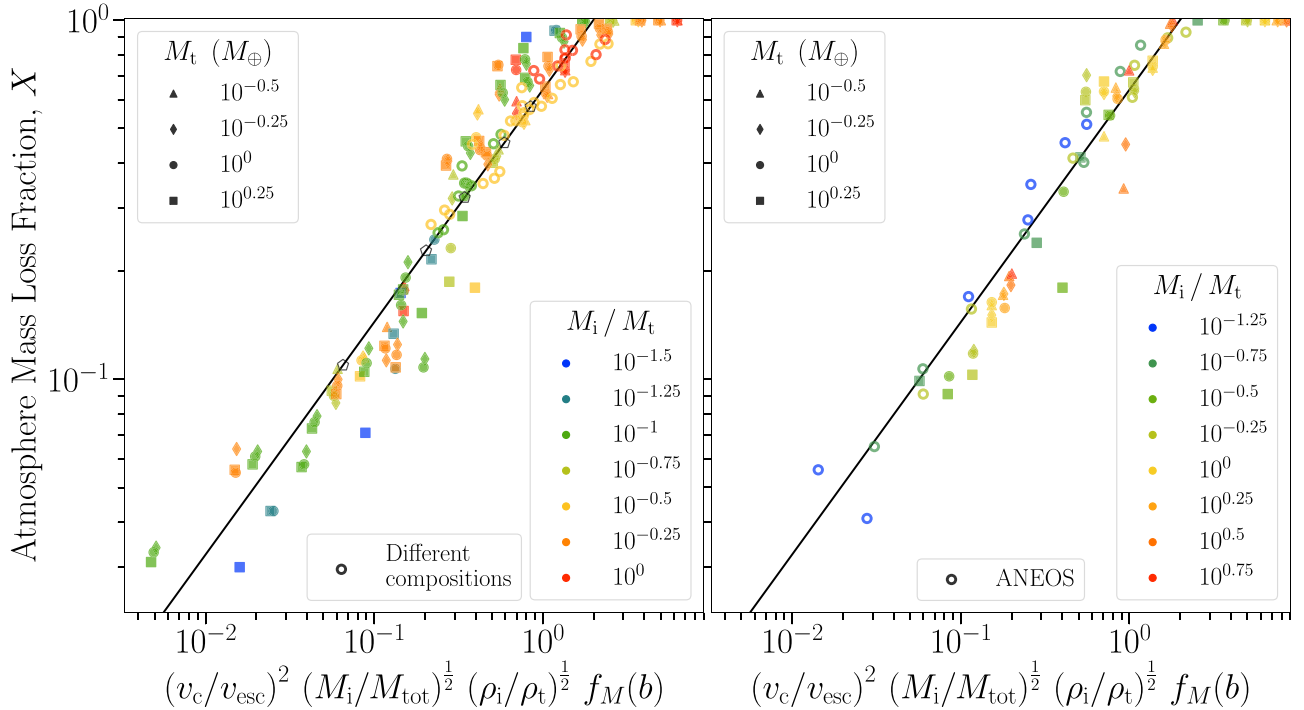


Figure 4. Left panel: lost mass fraction of the atmosphere from all of the standard simulation scenarios as a function of the scaling parameter, colored by the impactor:target mass ratio with markers set by the target mass. Open markers represent the third-suite impacts where one or both bodies are pure iron or pure rock. The black line shows our scaling law (Equation (1)). The black, open pentagons correspond to different Moon-forming impacts, as detailed in the text. Right panel: lost mass fraction of the atmosphere from (1) scenarios with atmosphere-hosting impactors (solid markers) including treating the impactor as the target to give impactor:target mass ratios larger than 1, and (2) scenarios for bodies with ANEOS forsterite mantles (open markers). These results are all presented numerically in Table 2.

In spite of the mass and composition differences between the target and impactor planets plus the dramatic qualitative differences between slow, fast, head-on, grazing, and intermediate scenarios, the median fractional deviation of the

simulated loss fractions from the scaling law is only 9%. The ubiquitous independence of the loss on the total system mass is illustrated by the overlapping clusters of same-color, different-shape points around the scaling line in Figure 4 (left panel).

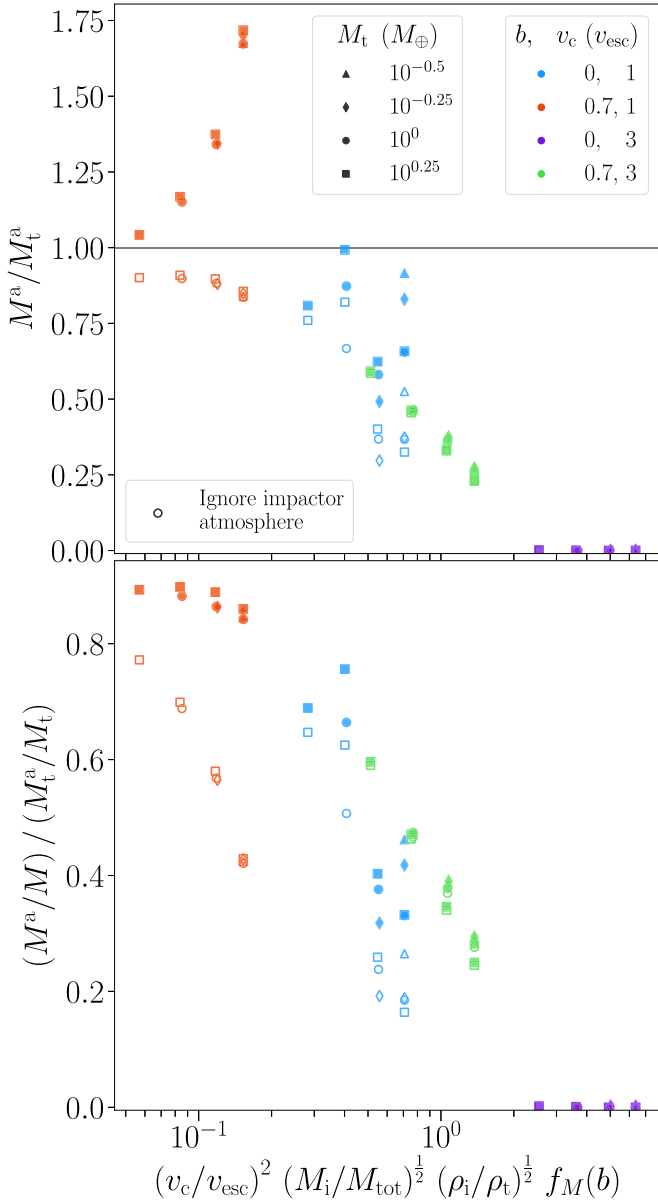


Figure 5. Top panel: the final bound atmosphere mass relative to the initial atmosphere mass of the target as a function of the scaling parameters, for scenarios with impactors that have $0.01M_i$ atmospheres, colored by the impact parameter and speed with markers set by the target mass. Open markers ignore the contribution of any atmosphere added by the impactor. Bottom panel: the final bound atmosphere mass as a fraction of the final core and mantle mass, relative to its initial value for the target.

(The data used to create this figure are available.)

We find that the specific impact energy ($\frac{1}{2}\mu v_c^2/M_{tot}$) is not the most convenient basis for a general scaling law. Instead, normalizing the speed at contact by the mutual escape speed allows scenarios with different masses and densities to be aligned by relatively simple additional terms. The scenarios in K20 also fit this trend well, with a similar scatter to those in this study.

Scenarios with $b = 0.7$ ($\beta = 44^\circ$) show the tightest fit to the scaling law (see also Figure A1). This is encouraging as 45° is the most common angle for a collision. The greatest

discrepancies arise from some of the (less common) head-on or highly grazing impacts, for which the loss changes with the scaling parameters more and less rapidly than the average trend, respectively. The slow, head-on scenarios also suffer from their significant chaotic uncertainty. To improve the fit for all angles would require that the power-law gradient be dependent on the angle. However, this would yield only a minor improvement to the already reasonable fit at the cost of losing the current simplicity.

The scaling law continues to agree well with the simulations that used the more sophisticated ANEOS EoS, as shown in Figure 4 (right panel). The median fractional difference in the atmospheric loss from the equivalent scenarios simulated using the Tillotson EoS is 2%.

Adding a thin atmosphere to the impactor does not affect significantly the fraction eroded from the target’s atmosphere (Figure 4, right panel). Furthermore, the scaling law still holds when the impactor is significantly more massive than the target.

The Moon-forming impact could have directly removed around 10 to 60% of an atmosphere across a range of plausible scenarios. In order of increasing loss, the example impacts shown in Figure 4 (left panel) are: canonical (Canup & Asphaug 2001), hit-and-run (Reufer et al. 2012, Figure 1(a)), large impactor (Canup 2012, Figure 1), fast-spinning Earth (Ćuk & Stewart 2012, Figure 1), and synestia (Lock et al. 2018, Figure 7).

3.3. Volatile Delivery by Atmosphere-hosting Impactors

If the impactor also has an atmosphere, then some may survive delivery to the final planet. For slow, grazing collisions the target can even end up with a larger atmosphere than it started with, typically $\sim 85\%$ of the combined mass of both initial atmospheres in these examples, as shown in Figure 5 (top panel). Slow, head-on impacts are less generous, but a large proportion of the atmosphere’s final composition can still come from the impactor. In the other subsets of much faster collisions tested here either the grazing impactor escapes the system along with most of its atmosphere or the entirety of both atmospheres are ejected regardless.

This limited set of scenarios demonstrates that giant impacts can significantly build as well as erode an atmosphere, but further study is required to make robust predictions across a wider range of scenarios and different initial masses for both atmospheres.

However, the relative atmosphere mass always decreases as a fraction of the planet’s total mass, as shown in Figure 5 (bottom panel). This demonstrates that although more atmosphere can be added than is removed, even more mantle and/or core material is added in any scenario. For the slow impactors that deliver significant atmosphere, $\sim 99\%$ of their core and mantle are also accreted. Planets thus inevitably end up with a smaller mass fraction of atmosphere following this kind of impact.

4. Conclusions: Applicability and Limitations

We have presented 3D simulations of giant impacts onto a range of terrestrial planets with thin atmospheres, including different masses, compositions and bulk densities, equations of state, speeds, and impact angles. We found a scaling law to

estimate the fraction of atmosphere lost from any collision in this regime (Equation (1)).

This scaling law has been shown to hold empirically for target and impactor masses ranging from roughly three times the Earth’s mass down to 0.3 and 0.05 of its mass, respectively; for differentiated and undifferentiated planets with densities from about half to over double the Earth’s density; and for any angle and speed. The atmospheric erosion is independent of the system mass for a fixed ratio of the impactor and target masses. Using the new ANEOS forsterite equation of state for the planets’ mantles instead of the crude Tillotson has a negligible effect on the resulting loss. We found no evident departure of the results from the trend at the extremes of these ranges, so it is plausible that the scaling applicability extends somewhat beyond.

The primary limitation for using this scaling law to make precise predictions elsewhere in the vast parameter space of giant impacts is the dependence on the atmosphere mass. Kegerreis et al. (2020, K20) found that the initial atmosphere mass has only a mild effect on the erosion in this regime of “thin” atmospheres, with $10\times$ lower mass leading to $\sim 10\%$ greater loss in their limited tests. It is possible that this trend could be accounted for with an extra term in the scaling law, but more focused study is required. Thicker atmospheres that are able to significantly cushion the impactor and alter its trajectory might require a more different scaling approach.

The temperature of the atmosphere is also relevant, and K20 found a similarly mild increase in loss for 1500 K warmer atmospheres. Comparable effects may be expected for different atmospheric compositions to the H–He used here, which would similarly affect the scale height. The longer-term thermal effects of a collision may cause additional loss (Biersteker & Schlichting 2019), the presence of an ocean beneath the atmosphere can increase the erosion (Genda & Abe 2005), and pre-impact rotation of the impactor and target could also cause significant differences (Ruiz-Bonilla et al. 2020).

Giant impacts can readily remove anywhere from almost none to all of an atmosphere. The strongest dependencies are on the angle and speed, as well as the masses of both bodies and, to a lesser extent, their densities. Slow impactors can also deliver a significant mass of atmosphere, but always accompanied by larger proportions of their mantle and core. Violent impacts can also erode the target’s mantle, typically removing at least $\sim 20\%$ for total atmospheric loss. Different Moon-forming impact scenarios correspond to the direct loss of from ~ 10 to 60% of a primordial atmosphere. This provides a new consideration for hypotheses of the Moon’s origin in combination with models for the history of Earth’s atmosphere.

Now that simulations like those presented here can be run with a high enough resolution to model the erosion of low-density atmospheres, future studies can probe the remaining unexplored regimes and investigate the impacts of smaller and even larger bodies. This way, robust scaling laws can continue to be built up to cover the full range of relevant scenarios in both our solar system and exoplanet systems for the loss and delivery of volatiles by giant impacts.

We thank the anonymous reviewer for their highly constructive comments. The research in this Letter made use of the SWIFT open-source simulation code (www.swiftsim.com; Schaller et al. 2018). This work was supported by the Science and Technology Facilities Council (STFC) grants ST/P000541/1 and ST/T000244/1, and used the DiRAC Data Centric system at Durham University, operated by the Institute

for Computational Cosmology on behalf of the STFC DiRAC HPC Facility (www.dirac.ac.uk). This equipment was funded by BIS National E-infrastructure capital grant ST/K00042X/1, STFC capital grants ST/H008519/1 and ST/K00087X/1, STFC DiRAC Operations grant ST/K003267/1 and Durham University. DiRAC is part of the National E-Infrastructure. J.A.K. acknowledges support from STFC grants ST/N001494/1 and ST/T002565/1. D.C.C., L.F.T.A., and K.J.Z. acknowledge support from NASA Planetary Atmospheres grant NNX14AJ45G. R.J.M. is supported by the Royal Society.

Software: SWIFT (www.swiftsim.com, Kegerreis et al. 2019; Schaller et al. 2016, version 0.8.5); WoMa (pypi.org/project/woma/, Ruiz-Bonilla et al. 2020).

Appendix A Initial Conditions and Impact Scenarios

The input parameters for each simulation are listed in Tables 1, 2, and 3, along with the resulting atmospheric erosion

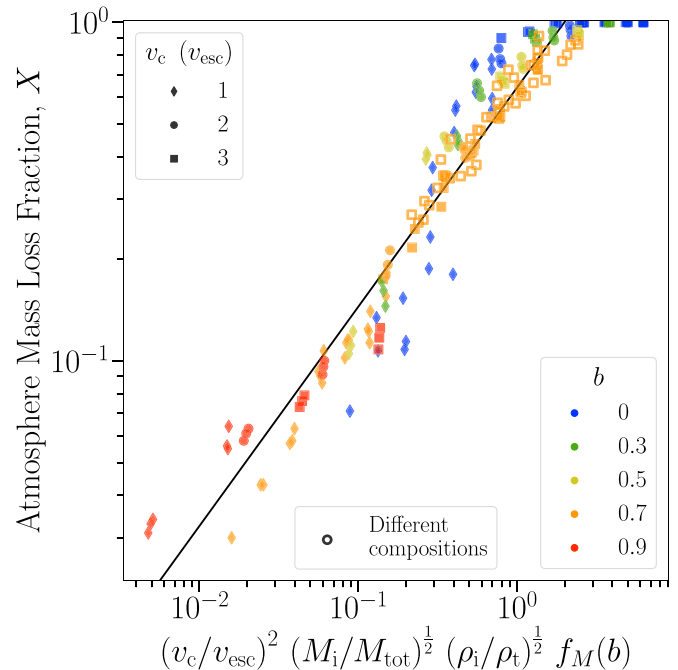


Figure A1. Same as Figure 4 (left panel) but colored instead by the impact parameter with markers set by the speed at contact.

Table 1
The Masses and Radii of the Bodies, Ignoring any Atmosphere

Standard		Same-mass		Same-radius	
Mass	Radius	Iron	Rock	Iron	Rock
(M_{\oplus})	(R_{\oplus})	(R_{\oplus})	(R_{\oplus})	(M_{\oplus})	(M_{\oplus})
$10^{-1.25}$	0.056	0.444			
10^{-1}	0.100	0.538	0.397	0.568	0.0782
$10^{-0.75}$	0.178	0.625			
$10^{-0.5}$	0.316	0.733	0.559	0.788	0.245
$10^{-0.25}$	0.562	0.856			
10^0	1.000	0.992	0.768	1.062	2.715
$10^{0.25}$	1.778	1.153			

Note. The bodies for the different-density suite are composed of pure iron or rock and either the standard mass or radius is kept the same, giving a new radius or mass, respectively.

Table 2
Simulation Scenarios

M_t (M_\oplus)	M_i (M_\oplus)	b	v_c (v_{esc})	X	M_t (M_\oplus)	M_i (M_\oplus)	b	v_c (v_{esc})	X	M_t (M_\oplus)	M_i (M_\oplus)	b	v_c (v_{esc})	X
<i>first suite</i>														
$10^{-0.5}$	$10^{-1.25}$	0	1	0.372	$10^{0.25}$	$10^{-1.25}$	0	3	0.898	10^0	$10^{-0.25}$	0	2	0.949
$10^{-0.5}$	$10^{-1.25}$	0.7	1	0.107	$10^{0.25}$	$10^{-1.25}$	0.7	3	0.174	10^0	$10^{-0.25}$	0.3	2	0.902
$10^{-0.5}$	$10^{-1.25}$	0	3	0.997	$10^{0.25}$	10^{-1}	0	1	0.134	10^0	$10^{-0.25}$	0.5	2	0.745
$10^{-0.5}$	$10^{-1.25}$	0.7	3	0.437	$10^{0.25}$	10^{-1}	0.7	1	0.043	10^0	$10^{-0.25}$	0.7	2	0.420
$10^{-0.5}$	10^{-1}	0	1	0.565	$10^{0.25}$	10^{-1}	0	3	0.935	10^0	$10^{-0.25}$	0.9	2	0.096
$10^{-0.5}$	10^{-1}	0.7	1	0.115	$10^{0.25}$	10^{-1}	0.7	3	0.216	10^0	$10^{-0.25}$	0.3	3	0.999
$10^{-0.5}$	10^{-1}	0	3	1.000	$10^{0.25}$	$10^{-0.75}$	0	1	0.153	10^0	$10^{-0.25}$	0.5	3	0.927
$10^{-0.5}$	10^{-1}	0.7	3	0.527	$10^{0.25}$	$10^{-0.75}$	0.7	1	0.057	$10^{0.25}$	$10^{-0.75}$	0.3	1	0.172
$10^{-0.5}$	$10^{-0.75}$	0	1	0.646	$10^{0.25}$	$10^{-0.75}$	0.7	3	0.285	$10^{0.25}$	$10^{-0.75}$	0.5	1	0.105
$10^{-0.5}$	$10^{-0.75}$	0.7	1	0.140	$10^{0.25}$	$10^{-0.5}$	0	1	0.187	$10^{0.25}$	$10^{-0.75}$	0.9	1	0.031
$10^{-0.5}$	$10^{-0.75}$	0	3	1.000	$10^{0.25}$	$10^{-0.5}$	0.7	1	0.093	$10^{0.25}$	$10^{-0.75}$	0	2	0.836
$10^{-0.5}$	$10^{-0.75}$	0.7	3	0.623	$10^{0.25}$	$10^{-0.5}$	0	3	0.998	$10^{0.25}$	$10^{-0.75}$	0.3	2	0.660
$10^{-0.5}$	$10^{-0.5}$	0	1	0.595	$10^{0.25}$	$10^{-0.5}$	0.7	3	0.401	$10^{0.25}$	$10^{-0.75}$	0.5	2	0.460
$10^{-0.5}$	$10^{-0.5}$	0.7	1	0.182	$10^{0.25}$	$10^{-0.25}$	0	1	0.180	$10^{0.25}$	$10^{-0.75}$	0.7	2	0.178
$10^{-0.5}$	$10^{-0.5}$	0	3	1.000	$10^{0.25}$	$10^{-0.25}$	0.7	1	0.102	$10^{0.25}$	$10^{-0.75}$	0.9	2	0.058
$10^{-0.5}$	$10^{-0.5}$	0.7	3	0.726	$10^{0.25}$	$10^{-0.25}$	0	3	1.000	$10^{0.25}$	$10^{-0.75}$	0.3	3	0.921
$10^{-0.25}$	$10^{-1.25}$	0	1	0.114	$10^{0.25}$	$10^{-0.25}$	0.7	3	0.528	$10^{0.25}$	$10^{-0.75}$	0.5	3	0.691
$10^{-0.25}$	$10^{-1.25}$	0.7	1	0.063	$10^{0.25}$	10^0	0	1	0.745	$10^{0.25}$	$10^{-0.75}$	0.9	3	0.073
$10^{-0.25}$	$10^{-1.25}$	0	3	0.992	$10^{0.25}$	10^0	0.7	1	0.124	$10^{0.25}$	10^0	0.3	1	0.461
$10^{-0.25}$	$10^{-1.25}$	0.7	3	0.347	$10^{0.25}$	10^0	0	3	1.000	$10^{0.25}$	10^0	0.5	1	0.394
$10^{-0.25}$	10^{-1}	0	1	0.319	$10^{0.25}$	10^0	0.7	3	0.653	$10^{0.25}$	10^0	0.9	1	0.056
$10^{-0.25}$	10^{-1}	0.7	1	0.086	$10^{0.25}$	$10^{0.25}$	0	1	0.776	$10^{0.25}$	10^0	0	2	0.978
$10^{-0.25}$	10^{-1}	0	3	0.997	$10^{0.25}$	$10^{0.25}$	0.7	1	0.155	$10^{0.25}$	10^0	0.3	2	0.943
$10^{-0.25}$	10^{-1}	0.7	3	0.418	$10^{0.25}$	$10^{0.25}$	0	3	1.000	$10^{0.25}$	10^0	0.5	2	0.790
$10^{-0.25}$	$10^{-0.75}$	0	1	0.550	$10^{0.25}$	$10^{0.25}$	0.7	3	0.758	$10^{0.25}$	10^0	0.7	2	0.429
$10^{-0.25}$	$10^{-0.75}$	0.7	1	0.115	<i>second suite</i>					$10^{0.25}$	10^0	0.9	2	0.091
$10^{-0.25}$	$10^{-0.75}$	0	3	1.000	$10^{-0.25}$	$10^{-1.25}$	0.3	1	0.145	$10^{0.25}$	10^0	0.3	3	0.998
$10^{-0.25}$	$10^{-0.75}$	0.7	3	0.518	$10^{-0.25}$	$10^{-1.25}$	0.5	1	0.122	$10^{0.25}$	10^0	0.5	3	0.946
$10^{-0.25}$	$10^{-0.5}$	0	1	0.621	$10^{-0.25}$	$10^{-1.25}$	0.9	1	0.034	$10^{0.25}$	10^0	0.9	3	0.108
$10^{-0.25}$	$10^{-0.5}$	0.7	1	0.113	$10^{-0.25}$	$10^{-1.25}$	0	2	0.756	<i>ANEOS forsterite mantles</i>				
$10^{-0.25}$	$10^{-0.5}$	0	3	1.000	$10^{-0.25}$	$10^{-1.25}$	0.3	2	0.601	$\dagger 10^0$	$10^{-1.25}$	0.7	1	0.041
$10^{-0.25}$	$10^{-0.5}$	0.7	3	0.616	$10^{-0.25}$	$10^{-1.25}$	0.5	2	0.427	$\dagger 10^0$	$10^{-1.25}$	0	2	0.513
$10^{-0.25}$	$10^{-0.25}$	0	1	0.550	$10^{-0.25}$	$10^{-1.25}$	0.7	2	0.212	$\dagger 10^0$	$10^{-1.25}$	0.3	2	0.456
$10^{-0.25}$	$10^{-0.25}$	0.7	1	0.179	$10^{-0.25}$	$10^{-1.25}$	0.9	2	0.063	$\dagger 10^0$	$10^{-1.25}$	0.5	2	0.349
$10^{-0.25}$	$10^{-0.25}$	0	3	1.000	$10^{-0.25}$	$10^{-1.25}$	0.3	3	0.872	$\dagger 10^0$	$10^{-1.25}$	0.7	2	0.170
$10^{-0.25}$	$10^{-0.25}$	0.7	3	0.723	$10^{-0.25}$	$10^{-1.25}$	0.5	3	0.658	$\dagger 10^0$	$10^{-1.25}$	0.9	2	0.056
10^0	$10^{-1.25}$	0	1	0.107	$10^{-0.25}$	$10^{-1.25}$	0.9	3	0.079	$\dagger 10^0$	$10^{-1.25}$	0.7	3	0.278
10^0	$10^{-1.25}$	0.7	1	0.043	$10^{-0.25}$	$10^{-0.5}$	0.3	1	0.444	$\dagger 10^0$	$10^{-0.75}$	0.7	1	0.107
10^0	$10^{-1.25}$	0	3	0.939	$10^{-0.25}$	$10^{-0.5}$	0.5	1	0.405	$\dagger 10^0$	$10^{-0.75}$	0	2	0.852
10^0	$10^{-1.25}$	0.7	3	0.245	$10^{-0.25}$	$10^{-0.5}$	0.9	1	0.064	$\dagger 10^0$	$10^{-0.75}$	0.3	2	0.720
10^0	10^{-1}	0	1	0.108	$10^{-0.25}$	$10^{-0.5}$	0	2	0.910	$\dagger 10^0$	$10^{-0.75}$	0.5	2	0.554
10^0	10^{-1}	0.7	1	0.058	$10^{-0.25}$	$10^{-0.5}$	0.3	2	0.883	$\dagger 10^0$	$10^{-0.75}$	0.7	2	0.254
10^0	10^{-1}	0	3	0.997	$10^{-0.25}$	$10^{-0.5}$	0.5	2	0.728	$\dagger 10^0$	$10^{-0.75}$	0.9	2	0.065
10^0	10^{-1}	0.7	3	0.324	$10^{-0.25}$	$10^{-0.5}$	0.7	2	0.397	$\dagger 10^0$	$10^{-0.75}$	0.7	3	0.402
10^0	$10^{-0.75}$	0	1	0.232	$10^{-0.25}$	$10^{-0.5}$	0.9	2	0.100	$\dagger 10^0$	$10^{-0.25}$	0.7	1	0.157
10^0	$10^{-0.75}$	0.7	1	0.090	$10^{-0.25}$	$10^{-0.5}$	0.3	3	0.999	$\dagger 10^0$	$10^{-0.25}$	0	2	0.926
10^0	$10^{-0.75}$	0	3	0.998	$10^{-0.25}$	$10^{-0.5}$	0.5	3	0.915	$\dagger 10^0$	$10^{-0.25}$	0.3	2	0.893
10^0	$10^{-0.75}$	0.7	3	0.411	$10^{-0.25}$	$10^{-0.5}$	0.9	3	0.125	$\dagger 10^0$	$10^{-0.25}$	0.5	2	0.749
10^0	$10^{-0.5}$	0	1	0.472	10^0	10^{-1}	0.3	1	0.161	$\dagger 10^0$	$10^{-0.25}$	0.7	2	0.413
10^0	$10^{-0.5}$	0.7	1	0.113	10^0	10^{-1}	0.5	1	0.111	$\dagger 10^0$	$10^{-0.25}$	0.9	2	0.091
10^0	$10^{-0.5}$	0	3	1.000	10^0	10^{-1}	0.9	1	0.033	$\dagger 10^0$	$10^{-0.25}$	0.7	3	0.610
10^0	$10^{-0.5}$	0.7	3	0.520	10^0	10^{-1}	0	2	0.778	<i>atmosphere-hosting impactors</i>				
10^0	$10^{-0.25}$	0	1	0.751	10^0	10^{-1}	0.3	2	0.628	$10^{-0.5}$	$*10^{-0.5}$	0	1	0.475
10^0	$10^{-0.25}$	0.7	1	0.122	10^0	10^{-1}	0.5	2	0.446	$10^{-0.5}$	$*10^{-0.5}$	0.7	1	0.161
10^0	$10^{-0.25}$	0	3	1.000	10^0	10^{-1}	0.7	2	0.192	$10^{-0.5}$	$*10^{-0.5}$	0	3	1.000
10^0	$10^{-0.25}$	0.7	3	0.624	10^0	10^{-1}	0.9	2	0.061	$10^{-0.5}$	$*10^{-0.5}$	0.7	3	0.738
10^0	10^0	0	1	0.727	10^0	10^{-1}	0.3	3	0.894	$10^{-0.25}$	$*10^{-0.5}$	0	1	0.703
10^0	10^0	0.7	1	0.177	10^0	10^{-1}	0.5	3	0.673	$10^{-0.25}$	$*10^{-0.5}$	0.7	1	0.120
10^0	10^0	0	3	1.000	10^0	10^{-1}	0.9	3	0.076	$10^{-0.25}$	$*10^{-0.5}$	0	3	1.000
10^0	10^0	0.7	3	0.726	10^0	$10^{-0.25}$	0.3	1	0.435	$10^{-0.25}$	$*10^{-0.5}$	0.7	3	0.634
$10^{0.25}$	$10^{-1.25}$	0	1	0.071	10^0	$10^{-0.25}$	0.5	1	0.411	$10^{-0.25}$	$*10^{-0.25}$	0	1	0.627
$10^{0.25}$	$10^{-1.25}$	0.7	1	0.030	10^0	$10^{-0.25}$	0.9	1	0.055	$10^{-0.25}$	$*10^{-0.25}$	0.7	1	0.151

Table 2
(Continued)

M_t (M_\oplus)	M_i (M_\oplus)	b	v_c (v_{esc})	X	M_t (M_\oplus)	M_i (M_\oplus)	b	v_c (v_{esc})	X	M_t (M_\oplus)	M_i (M_\oplus)	b	v_c (v_{esc})	X
$10^{-0.25}$	$*10^{-0.25}$	0	3	1.000	$10^{0.25}$	$*10^{-0.5}$	0.7	3	0.415	$*10^{-0.25}$	10^0	0	1	0.615
$10^{-0.25}$	$*10^{-0.25}$	0.7	3	0.732	$10^{0.25}$	$*10^{-0.25}$	0	1	0.180	$*10^{-0.25}$	10^0	0.7	1	0.173
10^0	$*10^{-0.5}$	0	1	0.333	$10^{0.25}$	$*10^{-0.25}$	0.7	1	0.091	$*10^{-0.25}$	10^0	0	3	1.000
10^0	$*10^{-0.5}$	0.7	1	0.102	$10^{0.25}$	$*10^{-0.25}$	0	3	1.000	$*10^{-0.25}$	10^0	0.7	3	0.871
10^0	$*10^{-0.5}$	0	3	1.000	$10^{0.25}$	$*10^{-0.25}$	0.7	3	0.545	$*10^{-0.5}$	$10^{0.25}$	0	1	0.725
10^0	$*10^{-0.5}$	0.7	3	0.543	$10^{0.25}$	$*10^0$	0	1	0.599	$*10^{-0.5}$	$10^{0.25}$	0.7	1	0.197
10^0	$*10^{-0.25}$	0	1	0.632	$10^{0.25}$	$*10^0$	0.7	1	0.103	$*10^{-0.5}$	$10^{0.25}$	0	3	0.998
10^0	$*10^{-0.25}$	0.7	1	0.118	$10^{0.25}$	$*10^0$	0	3	1.000	$*10^{-0.5}$	$10^{0.25}$	0.7	3	1.000
10^0	$*10^{-0.25}$	0	3	1.000	$10^{0.25}$	$*10^0$	0.7	3	0.671	$*10^{-0.25}$	$10^{0.25}$	0	1	0.451
10^0	$*10^{-0.25}$	0.7	3	0.644	$10^{0.25}$	$*10^{0.25}$	0	1	0.675	$*10^{-0.25}$	$10^{0.25}$	0.7	1	0.183
10^0	$*10^0$	0	1	0.633	$*10^{-0.5}$	$10^{-0.25}$	0.7	1	0.172	$*10^{-0.25}$	$10^{0.25}$	0	3	0.999
10^0	$*10^0$	0.7	1	0.164	$*10^{-0.5}$	$10^{-0.25}$	0.7	3	1.000	$*10^{-0.25}$	$10^{0.25}$	0.7	3	0.967
10^0	$*10^0$	0	3	1.000	$*10^{-0.5}$	$10^{-0.25}$	0.7	3	0.860	$*10^0$	$10^{0.25}$	0	1	0.604
10^0	$*10^0$	0.7	3	0.743	$*10^{-0.5}$	10^0	0	1	0.340	$*10^0$	$10^{0.25}$	0.7	1	0.158
$10^{0.25}$	$*10^{-0.5}$	0	1	0.240	$*10^{-0.5}$	10^0	0.7	1	0.194	$*10^0$	$10^{0.25}$	0	3	1.000
$10^{0.25}$	$*10^{-0.5}$	0.7	1	0.099	$*10^{-0.5}$	10^0	0	3	1.000	$*10^0$	$10^{0.25}$	0.7	3	0.882
$10^{0.25}$	$*10^{-0.5}$	0	3	0.999	$*10^{-0.5}$	10^0	0.7	3	0.978					

Note. The target mass, M_t , impactor mass, M_i , impact parameter, b , speed at contact, v_c , and lost mass fraction of the atmosphere, X , for the simulation scenarios, as presented in Figure 4. The second suite as described in Appendix A begins after the 88 first-suite simulations, not including any duplicates. Bodies with ANEOS forsterite mantles are indicated by a \dagger next to their masses. Additional first-suite scenarios with atmosphere-hosting impactors are indicated by a $*$ next to their mass, including scenarios where these impactors are treated as the targets to give impactor:target mass ratios greater than one.

(This table is available in machine-readable form.)

Table 3
Third-suite Simulations

M_i^{base} (M_\oplus)	Target		Impactor		X	M_i^{base} (M_\oplus)	Target		Impactor		X
	Mat.	Same	Mat.	Same			Mat.	Same	Mat.	Same	
10^{-1}			Iron	M	0.453	$10^{-0.5}$	Rock	M	Iron	R	0.858
10^{-1}			Rock	M	0.324	$10^{-0.5}$	Rock	M	Rock	R	0.524
10^{-1}	Iron	M			0.261	$10^{-0.5}$	Iron	R			0.288
10^{-1}	Iron	M	Iron	M	0.350	$10^{-0.5}$	Iron	R	Iron	M	0.451
10^{-1}	Iron	M	Rock	M	0.256	$10^{-0.5}$	Iron	R	Rock	M	0.296
10^{-1}	Rock	M			0.346	$10^{-0.5}$	Iron	R	Iron	R	0.649
10^{-1}	Rock	M	Iron	M	0.481	$10^{-0.5}$	Iron	R	Rock	R	0.270
10^{-1}	Rock	M	Rock	M	0.352	$10^{-0.5}$	Rock	R			0.576
10^{-1}	Iron	R	Iron	R	0.393	$10^{-0.5}$	Rock	R	Iron	M	0.674
10^{-1}	Rock	R	Rock	R	0.352	$10^{-0.5}$	Rock	R	Rock	M	0.590
$10^{-0.5}$			Iron	M	0.606	$10^{-0.5}$	Rock	R	Iron	R	0.860
$10^{-0.5}$			Rock	M	0.525	$10^{-0.5}$	Rock	R	Rock	R	0.542
$10^{-0.5}$			Iron	R	0.768	10^0			Iron	M	0.802
$10^{-0.5}$			Rock	R	0.478	10^0			Rock	M	0.746
$10^{-0.5}$	Iron	M			0.379	10^0	Iron	M			0.686
$10^{-0.5}$	Iron	M	Iron	M	0.553	10^0	Iron	M	Iron	M	0.786
$10^{-0.5}$	Iron	M	Rock	M	0.363	10^0	Iron	M	Rock	M	0.724
$10^{-0.5}$	Iron	M	Iron	R	0.747	10^0	Rock	M			0.824
$10^{-0.5}$	Iron	M	Rock	R	0.351	10^0	Rock	M	Iron	M	0.884
$10^{-0.5}$	Rock	M			0.564	10^0	Rock	M	Rock	M	0.827
$10^{-0.5}$	Rock	M	Iron	M	0.662	10^0	Iron	R	Iron	R	0.910
$10^{-0.5}$	Rock	M	Rock	M	0.578	10^0	Rock	R	Rock	R	0.782

Note. All of these scenarios are based on the $10^0 M_\oplus$ target with $b = 0.7$ and $v_c = 3 v_{esc}$. The remaining parameters are the base impactor mass, the material of each body, and whether their mass or radius was kept the same as the base version or left blank for a standard body with both materials.

(This table is available in machine-readable form.)

shown in Figures 4 and A1. The data shown in Figure 5 are available as data behind the figure.

For the first suite of changing masses, our four targets have masses of $10^{-0.5, -0.25, 0, 0.25} M_\oplus$, not including the atmospheres,

with up to seven impactor masses between $10^{-1.25} M_\oplus$ and the target's mass with the same logarithmic spacing of 0.25 dex, for a total of 22 target and impactor combinations. Table 1 lists these masses and corresponding radii. Each combination is

simulated in four scenarios: head-on, grazing, slow, and fast— $b = 0, 0.7$ and $v_c = 1, 3 v_{\text{esc}}$ —for a total of 88 simulations. For the four impactors with mass $\geq 10^{-0.5} M_{\oplus}$ we also run a duplicate simulation where the impactor also has an added atmosphere of 1% of its mass, for an extra 40 simulations. Furthermore, these atmosphere-hosting impactors can also be treated as the targets. This provides an additional set of scenarios for erosion by impactors that are more massive than the target.

For the second suite of changing speeds and angles, we select the impactors that are less massive than each target by 1 and 0.25 dex (with no atmospheres) for the three larger targets. In other words, the following six mass combinations (in M_{\oplus}) are used: $10^{-0.25}$ and $10^{-1.25, -0.5}$; 10^0 and $10^{-1, -0.25}$; $10^{0.25}$ and $10^{-0.75, 0}$. Each combination is simulated in scenarios with impact parameter $b = 0, 0.3, 0.5, 0.7, 0.9$ and speed at contact $v_c = 1, 2, 3 v_{\text{esc}}$ for a total of 90 simulations, out of which 24 are duplicates of the first suite.

For the third suite of different-density bodies, we take as a base a fast, grazing scenario ($b = 0.7$, $v_c = 3 v_{\text{esc}}$) with the $10^0 M_{\oplus}$ target and $10^{-1, -0.5, 0} M_{\oplus}$ impactors. These collisions yield middling erosion and tend to align closely with previous scaling laws (Kegerreis et al. 2020). For each of these default planets, we create new versions that are made entirely of iron or entirely of rock (instead of the default 30:70 mass ratio) keeping the same masses and allowing the radii to change, or keeping the same radii and allowing the masses to change, as listed in Table 1. We simulate the collision of each impactor with each target (skipping some combinations for the smallest and largest impactor, as detailed in Table 3), for a total of 47 simulations, out of which three are duplicates from the first two suites.

Finally, we run 21 additional simulations using the new ANEOS forsterite (Stewart et al. 2019) instead of Tillotson as the mantle material in both the targets and impactors. We collide $10^{-1.25, -0.75, -0.25} M_{\oplus}$ impactors with the $10^0 M_{\oplus}$ target, for $b = 0.7$ with $v_c = 1, 2, 3 v_{\text{esc}}$, and $b = 0, 0.3, 0.5, 0.7, 0.9$ with $v_c = 2 v_{\text{esc}}$.

To set the number of SPH particles in each simulation, for the smaller two targets we use 10^7 particles per $10^{-0.5} M_{\oplus}$ and for the larger two we use 10^7 particles per M_{\oplus} , giving particle masses of $3.2 \times 10^{-8} M_{\oplus} = 1.9 \times 10^{17}$ kg and $10^{-7} M_{\oplus} = 6.0 \times 10^{17}$ kg, respectively. This avoids the otherwise insufficient or unnecessarily high resolution for the smallest and largest targets if we had instead chosen a single particle mass throughout. The small downside is that two versions of most impactors must be created to match the particle mass of the target in each case.

In order to run the simulations until the amount of eroded material no longer changes significantly (see Kegerreis et al. 2020, their Figure 6), high-speed and/or low-angle scenarios with $v_c = 3$, or $v_c = 2$ and $b = 0, 0.3$, are run for 5 hr after contact, the others are run conservatively for 14 hr (plus the initial 1 hour before contact in both cases). The three simulations with $b = 0.9$, $v_c = 1 v_{\text{esc}}$, and an impactor:target mass ratio of $10^{-0.25}$ are exceptions and are stopped (in terms of their analysis) after 8.5 hr, before the nearly intact impactor fragment re-collides with the target. The double impacts in these unusual cases must be treated as separate collisions in order to follow the same scaling law as any other scenario. Snapshots of the particle data are output every 500 s.

Most simulations are run in the center-of-mass and zero-momentum frame. The exceptions are the high-speed, grazing impacts with massive impactors. The targets in these scenarios would rapidly exit the simulation box (of side length $80 R_{\oplus}$) as the unbound impactors fly out the opposite side. To avoid this, the following small subset of simulations are run instead in the initial rest frame of the target and in a larger $120 R_{\oplus}$ box: if (1) the impactor is either the same mass as the target or—for the larger two targets—0.25 dex less massive; and (2) $v_c \geq 2$ with $b \geq 0.5$.

Appendix B Approximate Interacting Mass

The fractional interacting mass, which for any impact angle loosely accounts for the proportions of the two bodies that interact, is given by

$$f_M \equiv \frac{\rho_t V_t^{\text{cap}} + \rho_i V_i^{\text{cap}}}{\rho_t V_t + \rho_i V_i}, \quad (\text{B1})$$

where $V_{t,i}$ are the total volumes of each body, ignoring any atmosphere, and $V_{t,i}^{\text{cap}}$ are the volumes of the target cap above the lowest point of the impactor at contact and the impactor cap below the highest point of the target, respectively. Both caps have height $d = (R_t + R_i)(1 - b)$, giving $V_{t,i}^{\text{cap}} = \frac{\pi}{3} d^2 (3R_{t,i} - d)$.

For equal bulk densities, this simplifies to the fractional interacting volume from Kegerreis et al. (2020, their Appendix B):

$$f_V \equiv \frac{V_t^{\text{cap}} + V_i^{\text{cap}}}{V_t + V_i} = \frac{1}{4} \frac{(R_t + R_i)^3}{R_t^3 + R_i^3} (1 - b)^2 (1 + 2b). \quad (\text{B2})$$

For the collisions in this study, f_M only differs from f_V by a median relative change of 2.5%.

ORCID iDs

J. A. Kegerreis  <https://orcid.org/0000-0001-5383-236X>
V. R. Eke  <https://orcid.org/0000-0001-5416-8675>
D. C. Catling  <https://orcid.org/0000-0001-5646-120X>
R. J. Massey  <https://orcid.org/0000-0002-6085-3780>
L. F. A. Teodoro  <https://orcid.org/0000-0002-8346-0138>
K. J. Zahnle  <https://orcid.org/0000-0002-2462-4358>

References

- Biersteker, J. B., & Schlichting, H. E. 2019, *MNRAS*, 485, 4454
Canup, R. M. 2012, *Sci*, 338, 1052
Canup, R. M., & Asphaug, E. 2001, *Natur*, 412, 708
Chambers, J. E. 2001, *Icar*, 152, 205
Ćuk, M., & Stewart, S. T. 2012, *Sci*, 338, 1047
Denman, T. R., Leinhardt, Z. M., Carter, P. J., & Mordasini, C. 2020, *MNRAS*, 496, 1166
Genda, H., & Abe, Y. 2005, *Natur*, 433, 842
Hubbard, W. B., & MacFarlane, J. J. 1980, *JGR*, 85, 225
Hwang, J., Chatterjee, S., Lombardi, James, J. J., Steffen, J. H., & Rasio, F. 2018, *ApJ*, 852, 41
Inamdar, N. K., & Schlichting, H. E. 2015, *MNRAS*, 448, 1751
Kegerreis, J. A., Eke, V. R., Gonnet, P., et al. 2019, *MNRAS*, 487, 1536
Kegerreis, J. A., Eke, V. R., Massey, R. J., & Teodoro, L. F. A. 2020, *ApJ*, 897, 161
Lammer, H., Leitzinger, M., Scherf, M., et al. 2020, *Icar*, 339, 113551
Liu, S.-F., Hori, Y., Lin, D. N. C., & Asphaug, E. 2015, *ApJ*, 812, 164

- Lock, S. J., Stewart, S. T., Petaev, M. I., et al. 2018, *JGRE*, **123**, 910
- Lopez, E. D., & Fortney, J. J. 2014, *ApJ*, **792**, 1
- Massol, H., Hamano, K., Tian, F., et al. 2016, *SSRv*, **205**, 153
- Melosh, H. J. 1989, *Impact cratering: A geologic process*, Oxford monographs on geology and geophysics (New York: Oxford Univ. Press)
- Ogihara, M., & Hori, Y. 2020, *ApJ*, **892**, 124
- Reufer, A., Meier, M. M. M., Benz, W., & Wieler, R. 2012, *Icar*, **221**, 296
- Ruiz-Bonilla, S., Eke, V. R., Kegerreis, J. A., Massey, R. J., & Teodoro, L. F. A. 2020, arXiv:2007.02965
- Sakuraba, H., Kurokawa, H., & Genda, H. 2019, *Icar*, **317**, 48
- Schaller, M., Gonnet, P., Chalk, A. B. G., & Draper, P. W. 2016, *Proc. PASC* 16, 2, 1
- Schaller, M., Gonnet, P., Chalk, A. B. G., & Draper, P. W. 2018, *SWIFT: SPH With Inter-dependent Fine-grained Tasking*, Astrophysics Source Code Library, arXiv:1805.020
- Schlichting, H. E., & Mukhopadhyay, S. 2018, *SSRv*, **214**, 34
- Stewart, S. T., Davies, E. J., Duncan, M. S., et al. 2019, arXiv:1910.04687
- Tillotson, J. H. 1962, *General Atomic Report*, GA-3216, 141
- Tucker, J. M., & Mukhopadhyay, S. 2014, *E&PSL*, **393**, 254
- Zahnle, K. J., Gacesa, M., & Catling, D. C. 2019, *GeCoA*, **244**, 56